Biomedical Optics EXPRESS

Distributed scanning volumetric SDOCT for motion corrected corneal biometry

Ryan P. McNabb,[1,*] Francesco LaRocca,[1] Sina Farsiu,[2,1] Anthony N. Kuo,[2] and Joseph A. Izatt[1,2]

[1]*Department of Biomedical Engineering, Duke University, 136 Hudson Hall, Box 90281, Durham, NC 27708, USA*
[2]*Department of Ophthalmology, Duke University Medical Center, Durham, NC 27710, USA*
**ryan.mcnabb@duke.edu*

Abstract: We present a method, termed distributed scanning OCT (DSOCT), which reduces the effects of patient motion on corneal biometry utilizing current-generation clinically available spectral domain optical coherence tomography (SDOCT) systems. We first performed a pilot study of the power spectrum of normal patient axial eye motion based on repeated (M-mode) SDOCT. Using DSOCT to reduce the effects of patient motion, we conducted a preliminary patient study comparing the measured anterior and posterior corneal curvatures and the calculated corneal power to both corneal topography and Scheimpflug photography in normal subjects. The repeatability for the measured radius of curvature of both anterior and posterior surfaces as well as calculated corneal refractive power using DSOCT was comparable to those of both topography and Scheimpflug photography.

OCIS codes: (110.4500) Optical coherence tomography; (170.4460) Ophthalmic optics and devices; (110.4153) Motion estimation and optical flow.

References and links

1. T. Olsen, "On the calculation of power from curvature of the cornea," Br. J. Ophthalmol. **70**(2), 152–154 (1986).
2. J. Schwiegerling, *Field Guide to Visual and Ophthalmic Optics* (SPIE, Bellingham, 2004).
3. B. Seitz, A. Langenbucher, N. X. Nguyen, M. M. Kus, and M. Küchle, "Underestimation of intraocular lens power for cataract surgery after myopic photorefractive keratectomy," Ophthalmology **106**(4), 693–702 (1999).
4. D. Huang, E. A. Swanson, C. P. Lin, J. S. Schuman, W. G. Stinson, W. Chang, M. R. Hee, T. Flotte, K. Gregory, C. A. Puliafito, and J. G. Fujimoto, "Optical coherence tomography," Science **254**(5035), 1178–1181 (1991).
5. J. A. Izatt, M. R. Hee, E. A. Swanson, C. P. Lin, D. Huang, J. S. Schuman, C. A. Puliafito, and J. G. Fujimoto, "Micrometer-scale resolution imaging of the anterior eye *in vivo* with optical coherence tomography," Arch. Ophthalmol. **112**(12), 1584–1589 (1994).
6. E. A. Swanson, J. A. Izatt, M. R. Hee, D. Huang, C. P. Lin, J. S. Schuman, C. A. Puliafito, and J. G. Fujimoto, "In vivo retinal imaging by optical coherence tomography," Opt. Lett. **18**(21), 1864–1866 (1993).
7. M. V. Sarunic, S. Asrani, and J. A. Izatt, "Imaging the ocular anterior segment with real-time, full-range Fourier-domain optical coherence tomography," Arch. Ophthalmol. **126**(4), 537–542 (2008).
8. C. K. S. Leung, W.-M. Chan, C. Y. Ko, S. I. Chui, J. Woo, M.-K. Tsang, and R. K. K. Tse, "Visualization of anterior chamber angle dynamics using optical coherence tomography," Ophthalmology **112**(6), 980–984 (2005).
9. V. Christopoulos, L. Kagemann, G. Wollstein, H. Ishikawa, M. L. Gabriele, M. Wojtkowski, V. Srinivasan, J. G. Fujimoto, J. S. Duker, D. K. Dhaliwal, and J. S. Schuman, "In vivo corneal high-speed, ultra high-resolution optical coherence tomography," Arch. Ophthalmol. **125**(8), 1027–1035 (2007).
10. K. Bizheva, N. Hutchings, L. Sorbara, A. A. Moayed, and T. Simpson, "In vivo volumetric imaging of the human corneo-scleral limbus with spectral domain OCT," Biomed. Opt. Express **2**(7), 1794–02 (2011).
11. M. Tang, Y. Li, M. Avila, and D. Huang, "Measuring total corneal power before and after laser in situ keratomileusis with high-speed optical coherence tomography," J. Cataract Refract. Surg. **32**(11), 1843–1850 (2006).
12. M. Zhao, A. N. Kuo, and J. A. Izatt, "3D refraction correction and extraction of clinical parameters from spectral domain optical coherence tomography of the cornea," Opt. Express **18**(9), 8923–8936 (2010).
13. A. N. Kuo, R. P. McNabb, M. Zhao, F. Larocca, S. S. Stinnett, S. Farsiu, and J. A. Izatt, "Corneal biometry from volumetric SDOCT and comparison with existing clinical modalities," Biomed. Opt. Express **3**(6), 1279–1290 (2012).

#168840 - $15.00 USD Received 21 May 2012; revised 8 Aug 2012; accepted 9 Aug 2012; published 10 Aug 2012

14. M. Tang, A. Chen, Y. Li, and D. Huang, "Corneal power measurement with Fourier-domain optical coherence tomography," J. Cataract Refract. Surg. **36**(12), 2115–2122 (2010).
15. "Device: RTVue Cam with Corneal Power Upgrade," (FDA, 2011), *http://www.accessdata.fda.gov/cdrh_docs/pdf11/K111505.pdf*.
16. S. Ortiz, D. Siedlecki, I. Grulkowski, L. Remon, D. Pascual, M. Wojtkowski, and S. Marcos, "Optical distortion correction in optical coherence tomography for quantitative ocular anterior segment by three-dimensional imaging," Opt. Express **18**(3), 2782–2796 (2010).
17. S. Ortiz, D. Siedlecki, P. Pérez-Merino, N. Chia, A. de Castro, M. Szkulmowski, M. Wojtkowski, and S. Marcos, "Corneal topography from spectral optical coherence tomography (sOCT)," Biomed. Opt. Express **2**(12), 3232–3247 (2011).
18. M. Gora, K. Karnowski, M. Szkulmowski, B. J. Kaluzny, R. Huber, A. Kowalczyk, and M. Wojtkowski, "Ultra high-speed swept source OCT imaging of the anterior segment of human eye at 200 kHz with adjustable imaging range," Opt. Express **17**(17), 14880–14894 (2009).
19. K. Karnowski, B. J. Kaluzny, M. Szkulmowski, M. Gora, and M. Wojtkowski, "Corneal topography with high-speed swept source OCT in clinical examination," Biomed. Opt. Express **2**(9), 2709–2720 (2011).
20. M. D. Robinson, S. J. Chiu, C. A. Toth, J. Izatt, J. Y. Lo, and S. Farsiu, "Novel applications of super-resolution in medical imaging," in *Super-Resolution Imaging,* P. Milanfar, ed. (CRC Press, 2010), pp. 383–412.
21. F. Ratliff and L. A. Riggs, "Involuntary motions of the eye during monocular fixation," J. Exp. Psychol. **40**(6), 687–701 (1950).
22. R. W. Ditchburn and B. L. Ginsborg, "Involuntary eye movements during fixation," J. Physiol. **119**(1), 1–17 (1953).
23. J. Otero-Millan, X. G. Troncoso, S. L. Macknik, I. Serrano-Pedraza, and S. Martinez-Conde, "Saccades and microsaccades during visual fixation, exploration, and search: foundations for a common saccadic generator," J. Vis. **8**(14), 21, 1–18 (2008).
24. S. H. Yun, G. Tearney, J. de Boer, and B. Bouma, "Motion artifacts in optical coherence tomography with frequency-domain ranging," Opt. Express **12**(13), 2977–2998 (2004).
25. R. Leitgeb, C. Hitzenberger, and A. Fercher, "Performance of fourier domain vs. time domain optical coherence tomography," Opt. Express **11**(8), 889–894 (2003).
26. M. Choma, M. Sarunic, C. Yang, and J. Izatt, "Sensitivity advantage of swept source and Fourier domain optical coherence tomography," Opt. Express **11**(18), 2183–2189 (2003).
27. J. F. de Boer, B. Cense, B. H. Park, M. C. Pierce, G. J. Tearney, and B. E. Bouma, "Improved signal-to-noise ratio in spectral-domain compared with time-domain optical coherence tomography," Opt. Lett. **28**(21), 2067–2069 (2003).
28. R. F. Spaide, H. Koizumi, and M. C. Pozonni, "Enhanced depth imaging spectral-domain optical coherence tomography," Am. J. Ophthalmol. **146**(4), 496–500 (2008).
29. F. La Rocca, S. J. Chiu, R. P. McNabb, A. N. Kuo, J. A. Izatt, and S. Farsiu, "Robust automatic segmentation of corneal layer boundaries in SDOCT images using graph theory and dynamic programming," Biomed. Opt. Express **2**(6), 1524–1538 (2011).
30. S. J. Chiu, X. T. Li, P. Nicholas, C. A. Toth, J. A. Izatt, and S. Farsiu, "Automatic segmentation of seven retinal layers in SDOCT images congruent with expert manual segmentation," Opt. Express **18**(18), 19413–19428 (2010).
31. V. Westphal, A. Rollins, S. Radhakrishnan, and J. Izatt, "Correction of geometric and refractive image distortions in optical coherence tomography applying Fermat's principle," Opt. Express **10**(9), 397–404 (2002).
32. R. P. McNabb, A. N. Kuo, M. Zhao, and J. A. Izatt, "Keratometric optical coherence tomography using fast distributed scan patterns," presented at *SPIE Photonics West*, San Francisco, CA, Jan. 23–28, 2010.
33. S. Farsiu, M. Elad, and P. Milanfar, "Constrained, globally optimal, multi-frame motion estimation," in *2005 IEEE/SP 13th Workshop on Statistical Signal Processing* (IEEE, 2005), pp. 1396–1401.
34. D. Malacara and Z. Malacara, *Handbook of Optical Design* (Marcel Dekker, 2004).
35. V. A. D. P. Sicam, M. Dubbelman, and R. G. L. van der Heijde, "Spherical aberration of the anterior and posterior surfaces of the human cornea," J. Opt. Soc. Am. A **23**(3), 544–549 (2006).
36. R. C. Lin, M. A. Shure, A. M. Rollins, J. A. Izatt, and D. Huang, "Group index of the human cornea at 1.3-μm wavelength obtained in vitro by optical coherence domain reflectometry," Opt. Lett. **29**(1), 83–85 (2004).
37. W. Drexler, C. K. Hitzenberger, A. Baumgartner, O. Findl, H. Sattmann, and A. F. Fercher, "Investigation of dispersion effects in ocular media by multiple wavelength partial coherence interferometry," Exp. Eye Res. **66**(1), 25–33 (1998).
38. D. A. Atchison and G. Smith, *Optics of the Human Eye* (Butterworth-Heinemann, 2000).
39. N. E. Norrby, "Unfortunate discrepancies," J. Cataract Refract. Surg. **24**(4), 433–434 (1998).
40. J. D. Ho, C. Y. Tsai, R. J. F. Tsai, L. L. Kuo, I. L. Tsai, and S. W. Liou, "Validity of the keratometric index: evaluation by the Pentacam rotating Scheimpflug camera," J. Cataract Refract. Surg. **34**(1), 137–145 (2008).
41. J. T. Holladay, W. E. Hill, and A. Steinmueller, "Corneal power measurements using scheimpflug imaging in eyes with prior corneal refractive surgery," J. Refract. Surg. **25**(10), 862–868 (2009).
42. L. Wang, A. M. Mahmoud, B. L. Anderson, D. D. Koch, and C. J. Roberts, "Total corneal power estimation: ray tracing method versus Gaussian optics formula," Invest. Ophthalmol. Vis. Sci. **52**(3), 1716–1722 (2011).

#168840 - $15.00 USD Received 21 May 2012; revised 8 Aug 2012; accepted 9 Aug 2012; published 10 Aug 2012

43. M. Tang, L. Wang, D. D. Koch, Y. Li, and D. Huang, "Intraocular lens power calculation after previous myopic laser vision correction based on corneal power measured by Fourier-domain optical coherence tomography," J. Cataract Refract. Surg. **38**(4), 589–594 (2012).
44. I. Grulkowski, M. Gora, M. Szkulmowski, I. Gorczynska, D. Szlag, S. Marcos, A. Kowalczyk, and M. Wojtkowski, "Anterior segment imaging with Spectral OCT system using a high-speed CMOS camera," Opt. Express **17**(6), 4842–4858 (2009).

1. Introduction

1.1. Corneal biometry with OCT

Accurate measurement of corneal topography and refractive power is important in determining the quality of vision, detection and diagnosis of pathology, prescription of noninvasive (corrective lens) and invasive (refractive surgery and cataract surgeries involving intraocular lenses) treatments, and evaluation of therapy efficacy. Placido ring-based corneal topography provides accurate values for the anterior surface of the cornea and calculates total corneal power under the assumption of a constant ratio between anterior and posterior corneal surface radii of curvature [1,2]. This power calculation is compromised when the ratio between surfaces may no longer be considered constant, such as in subjects who have undergone laser refractive surgery (e.g. LASIK, PRK) [3]. Rotating Scheimpflug photography based instruments (e.g. Oculus Pentacam®) estimate corneal refractive power, anterior and posterior radii of curvature, and corneal thickness from 25 to 50 full-diameter, radial photographs of the cornea.

First introduced over 20 years ago, optical coherence tomography (OCT) has become a robust imaging modality for micrometer-scale, noninvasive imaging in biological and biomedical applications [4]. The capacity for real-time noncontact, nonionizing *in vivo* imaging has fueled the investigation of this technique for applications in both anterior and posterior segment imaging in ophthalmology [5,6]. OCT offers the potential for full tomographic imaging of the cornea including micrometer-scale measurement of the anterior and posterior surfaces [5,7–10]. However, unavoidable patient motion during the time required for conventional OCT imaging may overwhelm the elevation accuracy required for clinically significant corneal curvature or refractive power calculations.

The first generation of anterior segment OCT systems used time-domain OCT (TDOCT) in various optical geometries. A study utilizing TDOCT with a 2 kHz A-scan rate reported a best achievable corneal power reproducibility of approximately 2 Diopters (D) [11], using a radial meridian scan pattern. We have recently demonstrated improved accuracy using 20 kHz spectral-domain OCT (SDOCT) with a scan pattern employing 50 radial meridians [12,13], however in this study we also observed undesirable variability between SDOCT measurements and reference values from standard instruments, likely resulting from patient motion artifacts during SDOCT acquisition. Such variability was shown to be reduced by another study utilizing a 26 kHz SDOCT system with only 8 meridians to cover the center 6 mm of the cornea [14]. This approach had the effect of reducing the total scan time, thus limiting the amount of patient motion and has since become cleared by the FDA for commercial use in humans [15]. However, this approach also comes at the expense of spatially under-sampling at the corneal periphery, potentially limiting its utility to characterizing low-order aberrations. Another publication described an OCT based corneal topography system which laterally under-sampled the cornea, however, because only anterior radii of curvatures were reported, this system will require more development to extend the biometry capabilities beyond those available from Placido-ring based topography [16,17]. Corneal power measurements have also been reported utilizing a high-speed swept source OCT (SS-OCT) system employing a Fourier domain mode locked (FDML) laser [18,19]. This system has the advantages of allowing for high speed acquisition, while not spatially under-sampling the center or periphery of the cornea. However, this system is currently a research prototype and requires considerable development for widespread clinical translation.

#168840 - $15.00 USD Received 21 May 2012; revised 8 Aug 2012; accepted 9 Aug 2012; published 10 Aug 2012

To reduce patient motion artifacts while preserving dense corneal sampling in a current-generation clinically available SDOCT system, we introduce a method which we term distributed scanning OCT (DSOCT). This method assumes that natural patient motion during SDOCT imaging is band-limited, and takes advantage of fast galvanometer motion to encode relatively slow patient motion into high spatial frequencies of a reconstructed image. The true corneal shape which is mostly free of motion artifact is then recovered by appropriate spatial filtering. This method may be considered as a multi-dimensional extension of the filtered cross-correlation scan registration technique for reduction of patient motion between A-scans, introduced for the earliest retinal OCT imaging by Swanson et al. [6]. By acquiring and then combining multiple under-sampled B-scans each acquired fast compared to patient motion, the technique also draws from super-resolution techniques developed by Farsiu et al. [20]. The distributed scanning technique could be applied as a software modification to widely available commercial SDOCT systems. The DSOCT approach also has the potential to scale up to higher speed/higher density scans with improved performance.

1.2. Patient motion considerations

In OCT, as in any axially symmetric optical system, it is convenient to categorize patient motion into orthogonal directions parallel (axial) and perpendicular (lateral) to the incident sample arm beam. Lateral motion may be due to voluntary head or eye motion, such as exploratory or voluntary saccades, or involuntary motion, such as microsaccades, tremors or drifts [21–23]. The amplitude and temporal characteristics of these motions are well characterized in the literature, and the majority of involuntary lateral eye motions are reported to occur at a rates of less than 100 Hz [21,23] and over short arc lengths (<1°) [23]. However, while lateral motions of a rotating spherical eyeball during OCT volume acquisition clearly lead to reduced lateral image resolution, axial patient motion may have a much more direct effect on errors in biometric parameters resulting from overall distortion of OCT images. For this reason, addressing biometry errors resulting from axial patient motion is the principal focus of this work. In previous work, axial eye motion has been reported to arise primarily from gross patient head motion, cardiac pulsations, and patient breathing [24]. However, the amplitude and frequency distribution of human eye axial motions are not well characterized in the literature. To provide a basis for selection of the parameters for our motion reduction approach, we conducted a pilot study of axial eye motion derived from analysis of repeated central corneal SDOCT A-scans in normal human volunteers under relaxed eye exam conditions.

2. Methods

2.1. Modified clinical SDOCT system

We acquired all data using a current-generation, commercial SDOCT system (Bioptigen, Inc.; Durham, NC) with a center wavelength λ of 840 nm and bandwidth $\Delta\lambda$ of 49 nm (Fig. 1). The axial resolution of the system was 6.2 μm in air and 4.5 μm in cornea (n_{gc} = *1.387*). The imaging depth of the system was 2.2 mm. The sensitivity of this system was measured to be 105 dB at an A-scan repetition rate of 20 kHz with 550 μW incident on the patient cornea. The portable commercial telecentric scanner was mounted on a modified slit-lamp base with a chin and forehead rest for subject stability. Software provided by Bioptigen, Inc. was used for real-time data detection, processing, display, and archiving, while custom software was used to apply a custom scan waveform to the galvanometers for beam scanning control. Each A-scan acquired had DC subtraction, dispersion compensation and FFT applied in real-time during acquisition.

Fourier domain OCT suffers from signal falloff due to finite sampling of the acquired spectra [25–27]. This issue results in a highest sensitivity close to the DC component of the Fourier transform, nearest the exact path length matching relative location of the reference

#168840 - $15.00 USD Received 21 May 2012; revised 8 Aug 2012; accepted 9 Aug 2012; published 10 Aug 2012

and sample arms. The signal and contrast of deep sample features can be enhanced relative to shallow sample features by locating the DC position below the object features of interest, a procedure denoted enhanced depth imaging (EDI) in retinal OCT [28]. We adapted this technique in all acquired volumes to improve the contrast of the corneal endothelium-aqueous boundary by placing the DC position below that boundary.

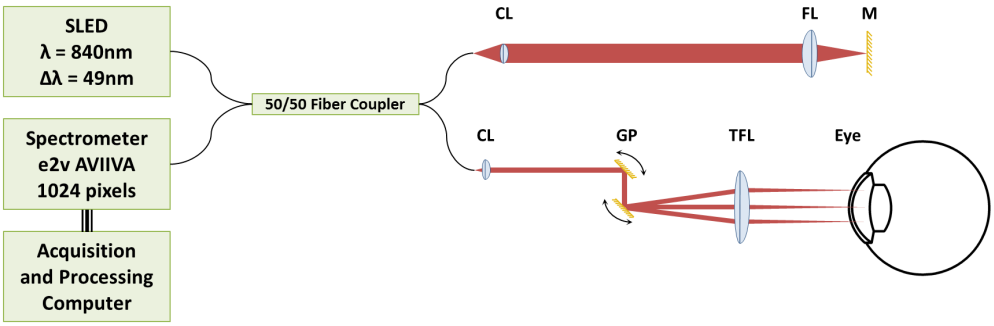

Fig. 1. Optical schematic of the commercial SDOCT system used. CL, collimating lens; FL, focusing lens; TFL, telecentric focusing lens; M, mirror; GP, orthogonal X-Y scanning galvanometer pair

2.2. Pilot study of normal patient axial eye motion

For the pilot study of axial eye motion, four normal human volunteers were imaged using the SDOCT system described in the previous section. Prior to imaging, informed consent was received for all subjects. The scan protocol consisted of a 40,000 M-mode scan with an integration time of 50 µs utilizing the device described above. Total scan time was 2 seconds with the position of the beam positioned near the vertex of the cornea. Two scans were performed on one eye for each subject. Motion was estimated by averaging the first 50 A-scans to create a kernel and cross-correlating the kernel with every A-scan to generate a one-dimensional vector containing the position of cornea at each A-scan. The resulting frequency amplitude spectra from all data sets were averaged and the standard deviations calculated at each frequency to create the power spectrum plot shown in the results (see Section 3.1).

2.3. Distributed scanning OCT

In a conventional OCT B-scan scan of an object, neighboring A-scans are acquired sequentially. Any sample motion that occurs during the acquisition of the B-scan is thus encoded into the data as spatial distortion or warping of the B-scan image. Thus, using conventional linear scanning it is difficult to discern which changes in apparent position of the subject are due to motion and which are due to the inherent shape of the imaged subject. Three-dimensional OCT volume acquisitions of samples are conventionally performed by acquiring multiple rapidly acquired A-scans while laterally scanning to create each B-scan, then acquiring multiple B-scans while azimuthally scanning to create a volume scan. Using such a linear scanning approach, any sample motion which occurs during data acquisition is also encoded directly as spatial variation in the B-scans. SDOCT volumes acquired using conventional linear raster scans, meridian radial scans, and annular scans all suffer from this motion-related artifact.

For distributed scanning OCT, we developed a scan pattern that allowed for spatially adjacent points to be temporally de-correlated, with a de-correlation time fast compared to the natural motion of the object over the time scale of interest. Based on the pilot study of axial eye motion reported in the results (see Section 3.1), which found axial eye motions of >1 µm in normal, relaxed patients to be band-limited to less than approximately 50 Hz, we considered any axial eye motion occurring in less than 10 ms to be negligible.

#168840 - $15.00 USD Received 21 May 2012; revised 8 Aug 2012; accepted 9 Aug 2012; published 10 Aug 2012

The basis for the custom scan pattern was a meridian radial scan. We chose this scan pattern for two reasons: 1) this pattern emphasized spatial sampling in the central region of the volume and 2) the central region of every B-scan, when centered and scanning a cornea, provided a high contrast region for post-processing and segmentation. The basis scan consisted of 20 meridian B-scans each with 500 A-scans and a depth of 1024 pixels with an integration time of 100 μs per A-scan. Starting with the location of the first A-scan of the first meridian (i.e., cutting horizontally across the sample) the meridians were subsampled, taking an A-scan at every 5th location of the basis radial scan until a single subsampled volume is acquired. This process started over at the location of the second A-scan of the first meridian, taking every 5th location and so on until all locations within the original basis scan pattern were acquired.

To cope with limitations imposed by inertia of the scanning mirrors, we designed the pattern to maximize sampling continuity. Thus, the tips of the 'petals' seen in the 'rosette' shaped scan pattern in Fig. 2 were not included in the final OCT volume, but instead were treated as inactive lines that were used to transfer from one meridian to another. The petal tips accounted for 10% of the total scan time. This approach had the advantage of allowing for a smooth scanning of the mirrors from meridian to meridian, but added a layer of complexity to reconstruction as even meridians were acquired in reverse with respect to the odd meridians.

For patient imaging, voluntary eye lateral motion was limited by asking the patient to stare at a stationary fixation target. An occluder was placed in front of the eye not being imaged to prevent fixation on any other targets. Gross patient head motion was limited by gently placing the subject's head against chin and forehead rests.

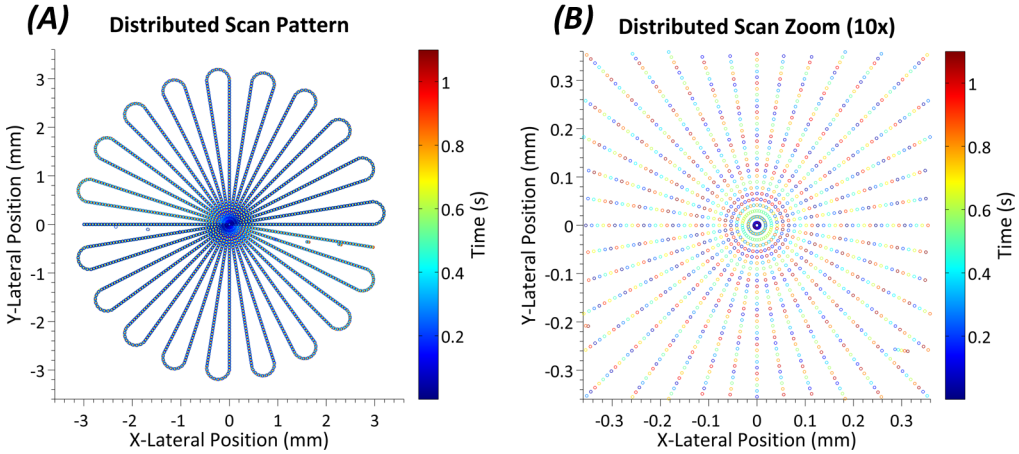

Fig. 2. (A) Distributed scan SDOCT pattern used in the study. Each point on the plot is in the correct lateral spatial location while the color of each point indicates the time at which it was taken. (B) A 10x zoom of the central region of the scan. Here the individual points can be distinguished. Note the distinctly different times at which spatially adjacent points are taken.

2.4. Reconstruction and segmentation

Because distributed scanning acquires A-scans linearly in time but not space, B-scans with correctly located A-scans were reconstructed in post-processing. Reconstruction was a fully automated multi-step process yielding a volume with 20 evenly spaced meridians of 420 A-scans each. Using our previously described corneal layer segmentation algorithm [29], based on our graph-theory and dynamic programming layer segmentation framework [30], we then segmented reconstructed volumes to find both the anterior and posterior surfaces in each meridian B-scan (see Fig. 3). This segmentation information had 3-D refraction correction applied [12,16,17], where curvature values and corneal thicknesses were recovered using

#168840 - $15.00 USD Received 21 May 2012; revised 8 Aug 2012; accepted 9 Aug 2012; published 10 Aug 2012

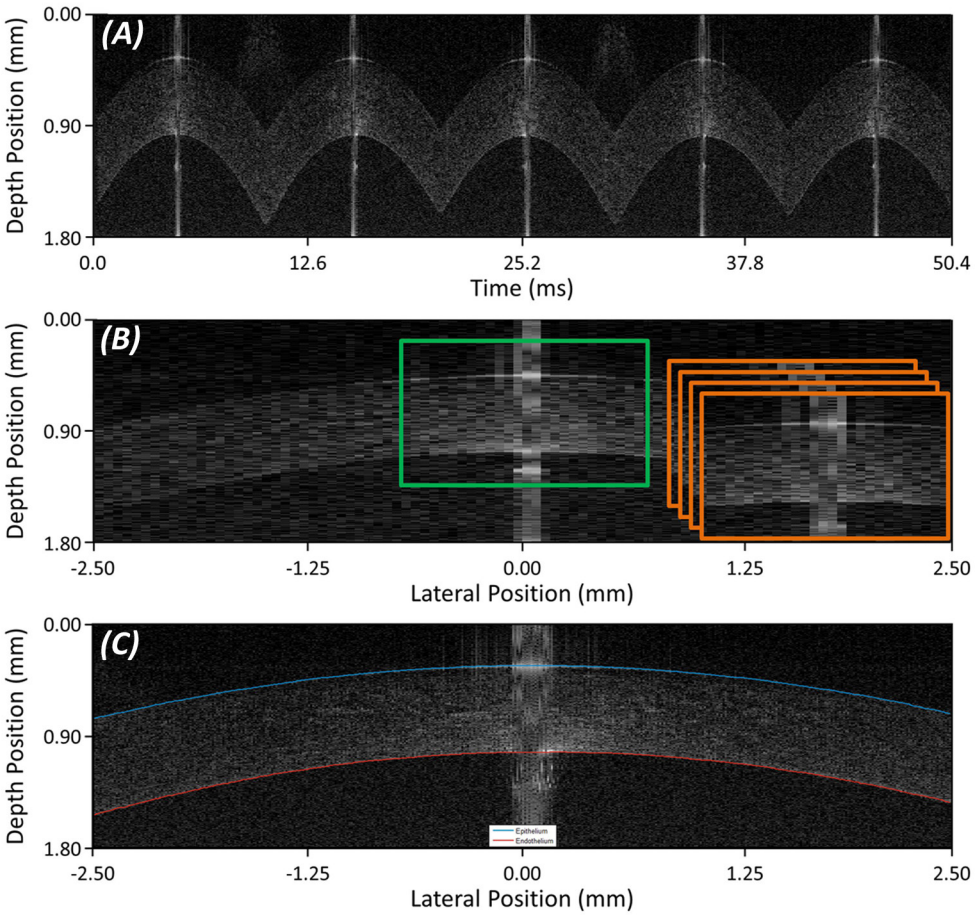

Fig. 3. (A) The first 540 lines of data acquired from the scan pattern illustrated in Fig. 2. Each small corneal profile contained 100 lines of data from 5 different radial slices. The full distributed volume was acquired in 1.1 seconds. (B) Each acquired corneal profile consisted of 100 active lines and 10 inactive lines. Five slightly offset profiles were used to reconstruct the final corneal slice. The centers of all five profiles of a given slice were automatically registered to one another to provide axial and lateral translation information. This was done for all twenty radial slices. (C) Using the information from the middle diagram, all A-scans were automatically shifted back to their correct axial and lateral positions to reconstruct all twenty meridians. The anterior and posterior surfaces were automatically segmented for all twenty meridians. This information was used to calculate the surface curvatures.

techniques as defined by Zhao et al. [12,31]. We used these recovered values to determine the refractive power of the corneas (see Section 2.5).

The reconstruction and transformation from a distributed scan acquisition to the desired basis meridian volume was a multi-step process. We implemented all post-processing algorithms in MATLAB (MathWorks; Natick, MA). The distributed scanning protocol used included 5 passes over 20 meridians creating 100 distinct corneal profiles. The first step of reconstruction was extracting these profiles from the acquired data and organizing them in a stack with respect to their associated meridian (i.e., the first five profiles in the stack belong to the first meridian; the next five belong to the second, etc.). Based on whether a meridian was odd or even, the corresponding profiles were unchanged or reversed left to right to account for the scan direction of the scan pattern. We corrected all profiles for 3 pixels of spatial delay per meridian due to the galvanometer mirror inertia and control circuit loop delay.

#168840 - $15.00 USD Received 21 May 2012; revised 8 Aug 2012; accepted 9 Aug 2012; published 10 Aug 2012

As stated earlier, the threshold that we considered to have no patient motion was on the order of 10 ms; each profile consisted of 100 A-scans acquired at 100 µs per A-scan yielding an acquisition time of 10 ms per profile [32]. Given this, we assumed that there was no significant motion in any given profile, while considering the motion that naturally exists (and is expected to be significant) between individual profiles. Corneal profiles within a given meridian were spatially (but not temporally) correlated. Using this spatial correlation, we were able to estimate and remove the motion that occurred between acquisitions.

For the next step in reconstruction, we assessed each meridian independently. First, we found the corneal apex in each of the profiles of a meridian. Following this, the anterior and posterior surfaces of the central portion of the corneal profile were segmented using previously described techniques [29]. We used these segmentation profiles to create two sets of masks for each meridian, one representing the location of the anterior surface and one for the posterior surface. We used these masks to find the relative movement (both axial and lateral motion across the individual meridian) between passes. The registration process was done twice for each meridian, once for anterior masks and once for posterior masks.

To minimize the overall motion estimation error, we exploited the bundle-adjusted multi-frame motion estimation framework [20,33]. In this framework, for a sequence of N meridian profiles, in the first step, we estimated all $N*(N-1)$ possible pairwise motion vector fields using cross-correlation. In the second step, (following [33], Section 3.2), these motion vectors were projected onto a consistent set of $N*(N-1)$ pairwise motion vectors, effectively reducing the motion estimation error between meridian profiles. The estimated motions for both the anterior and posterior surfaces in a set were then averaged to determine the final estimated motion for the set. Using this technique, we reconstituted all meridians to create a volume that was of the same form as the basis volume, in this case a meridian radial volume, which has also been motion corrected.

In the reconstructed volumes, we cropped the lateral edges of each meridian to remove empty A-scans generated from lateral motion and the galvanometer inertia correction previously applied. This left each meridian with 420 unique A-scans covering a distance of 5.04 mm. The anterior and posterior surfaces were then found using our automated segmentation algorithm [29]. The estimated surface topologies were then corrected for optical distortions due to nontelecentric scanning and refraction of the sample using our previously described methods [12] and were similar to those described by Ortiz, et al. [16,17].

2.5. Biometry

We used the acquired, optical distortion corrected meridian segmentations to calculate anterior and posterior corneal spherical curvature values. These were determined by least squares fitting of the three-dimensional surfaces to the equation for a conicoid of revolution where conic constant $k = 0$ to describe a sphere [34,35]:

$$\left(z - z_0\right) = \frac{c\left(\left(x - x_0\right)^2 + \left(y - y_0\right)^2\right)^2}{1 + \sqrt{1 - (1+k) * c^2 * \left(\left(x - x_0\right)^2 + \left(y - y_0\right)^2\right)^2}} \tag{1}$$

Here (x_0, y_0, z_0) represents the vertex of the surface, (x, y, z) points along the surface, and c is the inverse of the radius of curvature. Following the estimation of the curvature values for both the anterior and posterior surfaces of the cornea as well as the thickness in the center of the cornea, we determined the paraxial corneal power (inverse effective focal length) via the thick lens equation [1,11,13]:

$$\Phi_{TL} = \frac{n_c - n_a}{r_a} + \frac{n_q - n_c}{r_p} - \frac{CCT\left(n_c - n_a\right)\left(n_q - n_c\right)}{n_c r_a r_p} \tag{2}$$

#168840 - $15.00 USD Received 21 May 2012; revised 8 Aug 2012; accepted 9 Aug 2012; published 10 Aug 2012

The anterior and posterior radii of the inverse curvatures are represented by r_a and r_p respectively and the central corneal thickness is represented by *CCT*. For *CCT* and optical distortion correction of OCT images we used a value for the group refractive index of cornea which we reported in a previous study [13]. In that study, we experimentally calculated a corneal group refractive index n_{gc} = 1.387 at 840 nm using methods outlined in Lin, et al. [36]. This group refractive index was similar to the value calculated previously by Drexler et al. at 855 nm for cornea [37]. Phase refractive indices used for Gaussian optics calculations (i.e., power calculations) were the Gullstrand values found within the literature where the values for cornea, aqueous, and air were n_c = 1.376, n_q = 1.336, and n_a = 1.000, respectively [38]. Topography systems, however, only measure the front surface curvature and utilize a keratometric index, often given as n_k = 1.3375 to calculate refractive power [2]. This index assumes a fixed corneal thickness and fixed ratio between anterior and posterior surfaces. In addition, this index is referenced to the equivalent of the posterior vertex for the rear focal point instead of the rear principal plane as used in paraxial lens formulas [39]. To determine a 'keratometric equivalent power' (KEP) for DSOCT, we adapted the vertex power formula (inverse back focal length) to use the applicable ophthalmic variables [13]:

$$\Phi_{KEP} = \frac{n_c r_a * \Phi_{TL}}{n_c r_a - CCT\left(n_c - n_a\right)} \tag{3}$$

2.6. Validation phantoms

We used two types of phantoms to validate the extracted curvature values from reconstructed DSOCT volumes. All phantoms were scanned using the SDOCT system and scanning protocol described above. Post processing consisted of reconstruction and segmentation of applicable surfaces. All targets were laid flat against and imaged on a 3-axis translational stage with a ball joint stage for gross rotational alignment. The telecentric sample arm of the SDOCT system was mounted to a vertical translation stage allowing for simplified and stable acquisition of the targets.

First, we used reference glass spheres to validate a single curved surface in air simulating the corneal epithelium-air interface. The spheres used were designed for calibration of corneal topography machines. The second set of validation phantoms used consisted of rigid gas permeable (RGP) contact lenses (conformAthin; Conforma; Norfolk, VA) in air. To more closely mimic the physical configuration of the eye, we imaged the RGP contact lenses placed on rubber grommets that had a central clear aperture. Because the contact lenses were not mounted but instead simply placed on the grommets, they were measured in triplicate to validate repeatability in the event of any movement. We used the contact lenses to validate measuring the posterior surface and the central thickness of phantom, simulating the endothelial surface and the central thickness of the cornea respectively. For optical distortion correction, the refractive index of the contact lenses was provided by the manufacturer. We obtained measurements for both phantoms from a 5 mm zone.

2.7. DSOCT subject imaging

All human subject research was approved by the Duke University Medical Center Institutional Review Board. Prior to imaging, informed consent was received for all subjects after explanation of the possible consequences and nature of the study. All portions of this research followed the tenants of the Declaration of Helsinki.

The population for this preliminary study was drawn from healthy volunteers at the Duke Eye Center undergoing LASIK surgery for refraction correction. On the day of and prior to surgery, the subjects were imaged using corneal topography (Atlas 995®; Carl Zeiss Meditec Inc.; Dublin, CA), Scheimpflug photography (Pentacam® V2.73r19; Oculus Optikgeräte GmbH; Wetzlar, Germany), and the above described DSOCT technique. Scan parameters for Scheimpflug photography consisted of 25 radial meridians with a sample spacing of 0.1 mm

#168840 - $15.00 USD Received 21 May 2012; revised 8 Aug 2012; accepted 9 Aug 2012; published 10 Aug 2012

over 2 seconds. Scan parameters for DSOCT were as described in Section 2.3. Only eyes undergoing surgery were imaged and each imaging modality was done in triplicate for a given eye, providing a total of 9 measurements for each eye. The DSCOT volumetric data was post-processed as described in the above sections providing calculations for anterior corneal radius of curvature (r_a), posterior corneal curvature (r_p), central corneal thicknesses (CCT) and overall corneal refractive power for each imaged cornea over a 5 mm zone. For topography, r_a was equal to $337.5/\Phi_{SimK}$ where Φ_{SimK} was the reported spherical equivalent SimK value over a nominal 3 mm zone and 337.5 is equal to the keratometric constant, $1000*(n_k - n_a)$. For Scheimpflug photography, r_a and r_p were the mean reported radii of the anterior and posterior corneal surfaces, and CCT was the reported thickness at the apex. Refractive power, Φ_{EKR}, was the reported EKR value for the 3 mm zone. In addition, we calculated the keratometric equivalent power, as described above, for Scheimpflug photography using the reported anterior and posterior radii as well as the reported central corneal thickness. Each set of triplicate measurements was used to generate a mean value to compare each device in a pair-wise fashion. The standard deviation of the measurements from each triplicate set was used to denote the repeatability of an individual device.

3. Results

3.1. Axial eye motion pilot study

The results of the axial eye motion pilot study conducted in normal human volunteers are shown in Fig. 4. This study provided characterization of axial eye motion from 0.5 to 125 Hz. On average, axial eye motion within one standard deviation of 1 µm was band-limited to less than 25 Hz, and no patient exhibited motion of greater than 1 µm at 50 Hz.

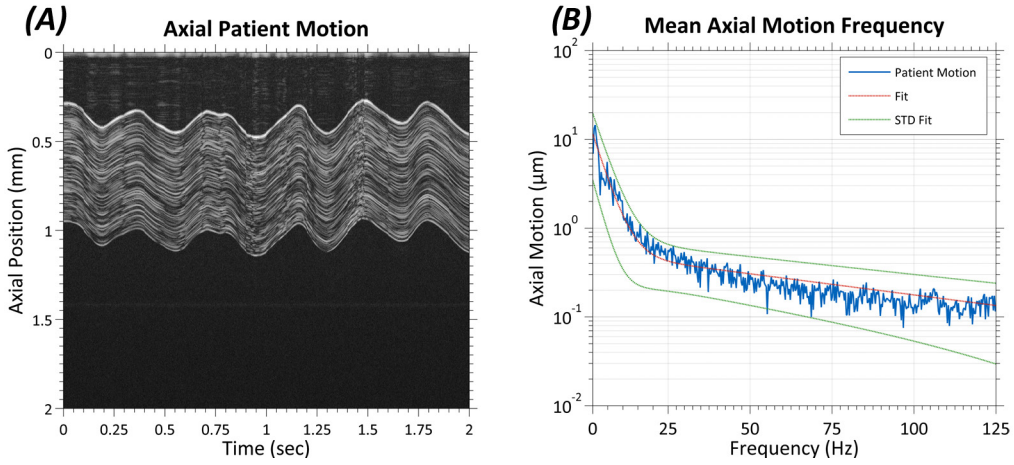

Fig. 4. Results from pilot patient axial motion study consisting of 4 subjects with 2 scans per subject. (A) Representative M-scan data comprising 40,000 repeated A-scans acquired at the same location near the apex of a subject's cornea. The integration time per A-scan was 50 µs, and the total acquisition time was 2 seconds. (B) Scaled average amplitude spectrum of the patient motion data. Axial patient motion drops below 1 µm amplitude for frequencies above ~25 Hz

3.2. Validation phantoms

The topography reference spheres used had manufacturer specified radii of 6.15 mm, 8.00 mm, and 9.65 mm, corresponding to a representative range of corneal anterior curvatures. The values measured with DSOCT were 6.150 mm, 7.999 mm, and 9.648 mm respectively. A representative reconstructed meridian is shown in Fig. 5A.

The RGP contact lenses used had manufacturer specified posterior radii of curvatures of 7.30 ± 0.02 mm, 7.70 ± 0.02 mm, and 8.20 ± 0.02 mm with each contact lens having a

#168840 - $15.00 USD Received 21 May 2012; revised 8 Aug 2012; accepted 9 Aug 2012; published 10 Aug 2012

specified thickness of 130 ± 20 μm. Results can be seen in Table 1 with the mean value and standard deviation of the results acquired in triplicate. A representative reconstructed meridian can be seen in Fig. 5B.

Table 1. DSOCT Measured Posterior Radii of Curvature (r_p) and Central Thicknesses for RGP Contact Lenses

RGP Contact Lens Manufacturer Specified Values		DSOCT Measured Values	
r_p (mm)	*Central Thickness* (μm)	r_p (mm)	*Central Thickness* (μm)
7.30 ± 0.02	130 ± 20	7.286 ± 0.005	132.8 ± 0.3
7.70 ± 0.02	130 ± 20	7.687 ± 0.004	134.8 ± 0.5
8.20 ± 0.02	130 ± 20	8.193 ± 0.001	140.7 ± 0.1

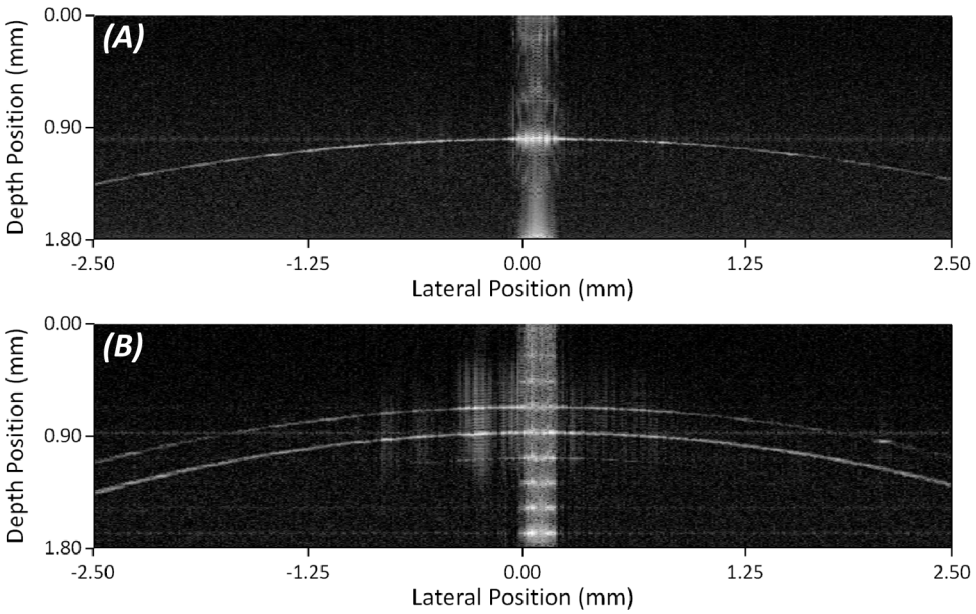

Fig. 5. (A) Single reconstructed meridian of 8.00 mm glass sphere phantom. (B) Single reconstructed meridian of 7.70 mm RGP contact.

3.3. Subject imaging

A total of 18 eyes from 10 subjects were imaged for the study. The mean age of the imaged subjects was 36.6 ± 9.3 years with a mean spherical equivalent manifest refraction of −3.48 ± 2.42 D. A total of 14 eyes from all 10 patients were used in the below comparisons. Four eyes were excluded from the study because at least one volume from the triplicate set was unusable due to corneal profiles not being present throughout the volume (i.e., patient blinked, portions of the cornea were off screen, etc.). Table 2 shows the average measured values for anterior radius for all three devices and the average posterior radius and central corneal thickness for both Scheimpflug photography and DSOCT for all 14 eyes. Table 3 provides the mean reported and calculated refractive power values for all three devices.

The average difference in refractive power between Topography and DSOCT was 0.086 ± 0.259D and the average difference between DSOCT and Scheimpflug photography was −0.003 ± 0.233D. For comparison the measured average difference between Scheimpflug photography and topography was −0.089 ± 0.265D. The average repeatability of the power measurements for each modality (topography, Scheimpflug photography, and DSOCT) were ±0.134D, ±0.142D, and ±0.092D respectively. Figures 6 and 7 compare the mean paired differences between the three devices for both corneal anterior radii of curvatures and corneal

#168840 - $15.00 USD Received 21 May 2012; revised 8 Aug 2012; accepted 9 Aug 2012; published 10 Aug 2012

refractive power. The mean paired differences between DSOCT and both topography and Scheimpflug photography were comparable to the mean paired differences between topography and Scheimpflug photography.

Table 2. Measured Anterior and Posterior Curvatures and Central Corneal Thicknesses

Subject	***Topography***	***Scheimpflug Photography***			***DSOCT***		
(Eye)	r_a (mm)	r_a (mm)	r_p (mm)	*CCT* (μm)	r_a (mm)	r_p (mm)	*CCT* (μm)
Sub1 (OD)	7.288 ± 0.017	7.377 ± 0.081	6.267 ± 0.035	535 ± 19.1	7.389 ± 0.001	6.591 ± 0.011	537 ± 1.2
Sub1 (OS)	7.348 ± 0.027	7.340 ± 0.017	6.223 ± 0.038	525 ± 5.5	7.376 ± 0.012	6.604 ± 0.019	532 ± 1.5
Sub2 (OD)	7.606 ± 0.011	7.590 ± 0.000	6.340 ± 0.036	634 ± 3.0	7.599 ± 0.013	6.710 ± 0.042	630 ± 1.1
Sub2 (OS)	7.664 ± 0.007	7.627 ± 0.006	6.420 ± 0.020	634 ± 6.8	7.660 ± 0.011	6.694 ± 0.017	632 ± 0.2
Sub3 (OD)	7.830 ± 0.013	7.807 ± 0.021	6.650 ± 0.095	554 ± 5.3	7.867 ± 0.009	7.049 ± 0.017	544 ± 1.4
Sub3 (OS)	7.834 ± 0.007	7.800 ± 0.010	6.807 ± 0.065	557 ± 1.7	7.873 ± 0.024	7.083 ± 0.007	550 ± 1.1
Sub4 (OD)	7.560 ± 0.016	7.543 ± 0.032	6.190 ± 0.061	599 ± 4.6	7.568 ± 0.018	6.563 ± 0.015	599 ± 0.9
Sub4 (OS)	7.539 ± 0.012	7.490 ± 0.026	6.167 ± 0.029	599 ± 5.3	7.541 ± 0.011	6.496 ± 0.004	595 ± 1.2
Sub5 (OS)	7.973 ± 0.014	7.953 ± 0.006	6.690 ± 0.046	515 ± 6.1	8.013 ± 0.026	7.102 ± 0.013	518 ± 1.6
Sub6 (OS)	7.733 ± 0.017	7.773 ± 0.006	6.507 ± 0.038	509 ± 4.7	7.737 ± 0.021	6.851 ± 0.024	514 ± 0.5
Sub7 (OD)	8.028 ± 0.025	8.030 ± 0.010	6.693 ± 0.025	572 ± 3.5	8.030 ± 0.008	7.056 ± 0.016	575 ± 6.1
Sub8 (OS)	8.237 ± 0.117	8.117 ± 0.006	6.627 ± 0.006	560 ± 7.8	8.146 ± 0.006	7.066 ± 0.031	549 ± 2.3
Sub9 (OS)	7.850 ± 0.041	7.797 ± 0.015	6.370 ± 0.020	527 ± 4.0	7.766 ± 0.007	6.858 ± 0.030	524 ± 1.4
Sub10 (OD)	7.918 ± 0.023	7.877 ± 0.015	6.390 ± 0.046	595 ± 5.7	7.851 ± 0.033	6.844 ± 0.077	592 ± 2.7
Mean	7.743	7.723	6.460	566	7.744	6.826	564
Mean Repeatability	0.025	0.018	0.040	5.9	0.014	0.023	1.6

Table 3. Power Calculations

Subject	***Topography***	***Scheimpflug Photography***		***DSOCT***	
(Eye)	Φ_{SimK} (D)	Φ_{EKR} (D)	Φ_{KEP} (D)	Φ_{TL} (D)	Φ_{KEP}(D)
Sub1 (OD)	46.31 ± 0.107	45.93 ± 0.379	45.62 ± 0.516	44.94 ± 0.004	45.85 ± 0.006
Sub1 (OS)	45.93 ± 0.166	46.00 ± 0.100	45.82 ± 0.097	45.04 ± 0.068	45.94 ± 0.071
Sub2 (OD)	44.37 ± 0.063	44.77 ± 0.058	44.39 ± 0.041	43.66 ± 0.057	44.67 ± 0.061
Sub2 (OS)	44.04 ± 0.038	44.33 ± 0.058	44.22 ± 0.051	43.24 ± 0.086	44.24 ± 0.089
Sub3 (OD)	43.10 ± 0.072	43.17 ± 0.208	43.10 ± 0.169	42.23 ± 0.063	43.04 ± 0.066
Sub3 (OS)	43.08 ± 0.038	43.33 ± 0.115	43.29 ± 0.121	42.22 ± 0.143	43.04 ± 0.149
Sub4 (OD)	44.64 ± 0.094	44.67 ± 0.153	44.49 ± 0.191	43.72 ± 0.131	44.69 ± 0.135
Sub4 (OS)	44.77 ± 0.072	44.83 ± 0.252	44.84 ± 0.178	43.84 ± 0.074	44.81 ± 0.075
Sub5 (OS)	42.33 ± 0.074	42.33 ± 0.153	42.15 ± 0.023	41.39 ± 0.144	42.14 ± 0.147
Sub6 (OS)	43.64 ± 0.094	43.37 ± 0.115	43.11 ± 0.012	42.86 ± 0.116	43.66 ± 0.121
Sub7 (OD)	42.04 ± 0.131	41.97 ± 0.115	41.78 ± 0.082	41.27 ± 0.056	42.09 ± 0.051
Sub8 (OS)	40.98 ± 0.577	41.66 ± 0.115	41.27 ± 0.025	40.60 ± 0.028	41.36 ± 0.028
Sub9 (OS)	43.00 ± 0.224	42.93 ± 0.058	42.85 ± 0.098	42.69 ± 0.026	43.50 ± 0.029
Sub10 (OD)	42.62 ± 0.123	42.83 ± 0.115	42.48 ± 0.122	42.17 ± 0.267	43.05 ± 0.280
Mean	43.63	43.72	43.53	42.85	43.72
Mean Repeatability	0.134	0.142	0.122	0.090	0.093

4. Discussion

Utilizing an SDOCT system that is clinically available, we have developed a technique, termed DSOCT, which reduces the effects of patient motion in corneal tomographic data for the generation of clinically relevant corneal biometric information. DSOCT was developed in response to our prior experience using conventional radial scan patterns for corneal biometry. On a population similar to the one described in the current work, we found that inter-device bias for SDOCT compared well to topography and Scheimpflug photography devices but the inter-device variability for SDOCT was higher than 0.50 D [13]. One potential source for this variability was axial subject motion during OCT image acquisition.

We characterized axial subject motion by performing a pilot study that provided preliminary characterization of human eye axial motion from 0.5 to 125 Hz. This pilot study indicated that motions of >1 μm, sufficient to distort biometric measurements according to prior reports [14], were indeed band-limited to less than approximately 50 Hz. This pilot study did not address tear film dynamics due to the ~5 μm axial resolution of our system. These

#168840 - $15.00 USD Received 21 May 2012; revised 8 Aug 2012; accepted 9 Aug 2012; published 10 Aug 2012

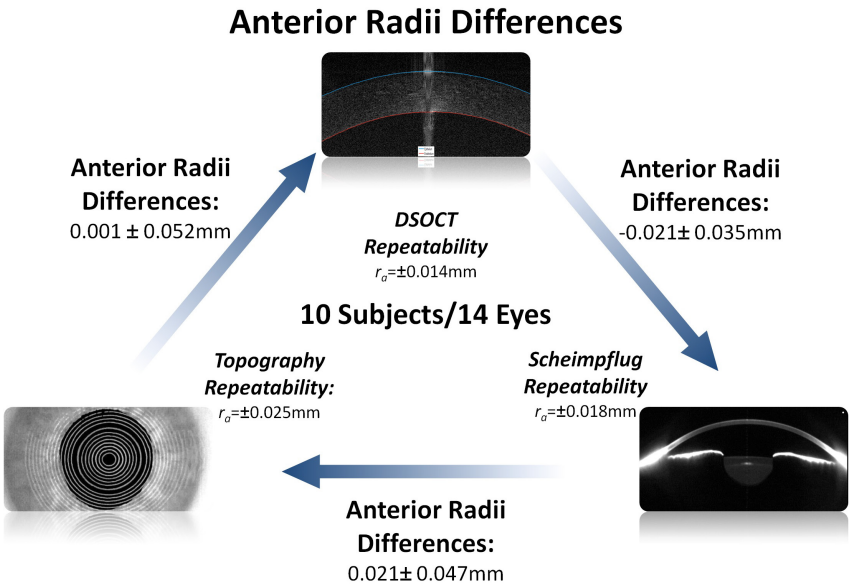

Fig. 6. Comparison between DSOCT, topography and Scheimpflug photography for measured corneal anterior surface radii of curvatures. Shown differences are the mean and standard deviation of paired differences between devices. Starting from the bottom left and going clockwise: Topography – DSOCT; DSOCT – Scheimpflug photography; Scheimpflug photography – Topography

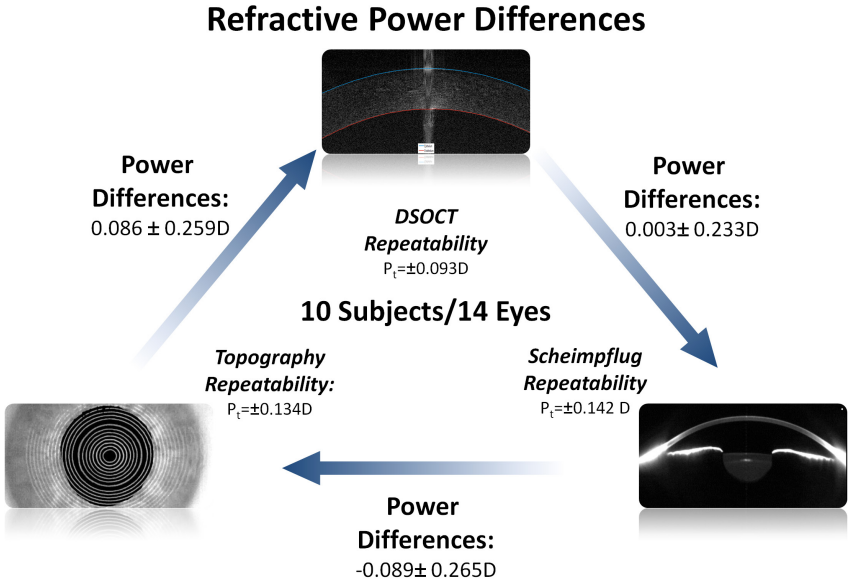

Fig. 7. Comparison between DSOCT, topography and Scheimpflug photography for reported and calculated corneal refractive power. Shown differences are the mean and standard deviation of paired differences between devices. Starting from the bottom left and going clockwise: Topography – DSOCT; DSOCT – Scheimpflug photography; Scheimpflug photography – Topography

results provided a quantitative target for our selection of a cut-off frequency between natural patient motion and artificial (apparent) motion we induced by distributed scanning, which we set conservatively at 100 Hz. For this pilot study, we made the assumption that we were only measuring axial motion. Because we imaged near the vertex of the cornea and had the

#168840 - $15.00 USD Received 21 May 2012; revised 8 Aug 2012; accepted 9 Aug 2012; published 10 Aug 2012

subjects fixate on a target, small lateral motion should result in very small changes in apparent axial motion which would be overwhelmed by actual axial motion. For this assumption to remain true, a two second scan time was a relatively long scan time. This was a compromise between having a scan that wasn't too long and one that contained enough data to provide the low-frequency information we required.

Following this pilot study, DSOCT was then tested on two sets of phantoms: calibration spheres for corneal topography and rigid gas permeable contact lenses. These tests confirmed that we could accurately reconstruct surface data of varying curvatures even through an intervening medium in the case of the contact lenses. For both sets, measurements acquired using DSOCT matched well with manufacturer supplied specifications.

We then applied DSOCT in a clinical setting on a normal patient population undergoing LASIK refractive correction surgery. This environment provided the opportunity to obtain repeated measurements from not only DSOCT but corneal topography and Scheimpflug photography as well for comparison. Values for anterior and posterior radii of curvature as well as central corneal thickness were acquired directly from DSOCT tomographic data. Experimentally, we found that a 5 mm zone best agreed with our reference calibration targets. With this experience, we chose to use this fitting zone consistently in the clinical scans as well. In prior work, the resultant clinical measurements correlated well with other clinical platforms despite this zone [13]. We acknowledge that the cornea is generally assumed to be spherical around a 3 mm zone, but chose to prioritize the experimental calibration data. For the anterior corneal surface, there was good agreement between all three devices. While topography does not report a value for central corneal thickness, there was a good agreement between DSOCT and Scheimpflug photography with a mean difference of less than 2 μm or less than 0.32%. In addition, topography does not measure or report posterior curvature. Regarding posterior curvatures, DSOCT and Scheimpflug photography were in disagreement with a mean difference of over 0.35 mm or more than 5%. The final consideration that we made was the average ratio between the posterior and anterior surfaces of the cornea (r_p/r_a). Topography, using the Gullstrand model, assumes a ratio of 0.88 while other studies have shown Pentacam, the device we used for Scheimpflug photography measurements, to have a ratio of 0.82 ± 0.02 [40,41]. Our population had a Scheimpflug photography ratio of 0.837 ± 0.016 and a DSOCT ratio of 0.881 ± 0.012.

Unlike the anterior surface which consists of an air-tissue interface that is directly accessible by optical devices, the posterior surface may only be observed *in vivo* by imaging through tissue. This in turn requires that multiple assumptions are made to estimate its radius of curvature. Our group used an experimentally measured index of refraction and three dimensional optical distortion correction to locate the posterior surface (see Section 2.5) [12,13]. Unfortunately, we do not know the indices of refraction used by Pentacam or if they utilize a two or three dimensional refraction correction technique. We do know that they utilize a formula to calculate power (EKR) which is benchmarked to keratometry and scales the posterior radius to do so [41]. These differences may be the source of this discrepancy. Aside from the above, the posterior radius of curvature is higher in our population for both DSOCT and Scheimpflug photography. Given the small sample size in our study a few subjects with larger than average posterior curvature values (subjects 3, 5, 7 & 8) may greatly influence the overall mean value.

The mean reported SimK refractive power for topography was 43.63D and a mean repeatability of ±0.134. The mean reported EKR refractive power for Scheimpflug photography was 43.72D and a mean repeatability of ±0.142D. This resulted in a bias of only 0.089D between these two devices. Using the measured values reported above, we calculated the corneal refractive power using the Eq. (2) for DSOCT. The mean refractive power calculated for DSOCT using Eq. (2) was 42.85D with a mean repeatability of ±0.090. While mean repeatability was comparable to the other devices, there was a bias of 0.786D and 0.875D to topography and Scheimpflug photography, respectively. Topography however does

#168840 - $15.00 USD Received 21 May 2012; revised 8 Aug 2012; accepted 9 Aug 2012; published 10 Aug 2012

not use the paraxial corneal power but is instead referenced to the vertex. With a Gullstrand model eye, the difference between paraxial and vertex power calculations is ~0.8D [14,42]. To match our values with the reported values of topography, we used the KEP power calculation, Eq. (3), to determine corneal refractive power for DSOCT. The mean refractive power calculated for DSOCT using this KEP was 43.72D with a mean repeatability of ±0.093D. Again we had a comparable mean repeatability to the other devices but the bias was substantially improved to −0.086D and −0.003D for topography and Scheimpflug photography, respectively. We also used the reported curvature and thickness values from Scheimpflug photography and calculated the associated KEP power values. Here we saw a reduction in the mean power by ~0.2D with little change in the repeatability. Because anterior surface values are similar for topography and Scheimpflug photography, this change in power is likely due to the lower reported mean posterior curvature values.

Clinical devices provide corneal refractive power through differing measurements and calculations. Despite these differences however, it is important to provide a corneal power value that can be used for clinical purposes (i.e., intraocular lens power calculations [43]). Traditionally, the corneal refractive power value was measured from a keratometer with its attendant limitations. The SimK and EKR values from topography and Scheimpflug photography respectively provide "keratometer like" values that can be used in lieu of measurements from an actual keratometer. Even if not exactly equivalent, these analogous values should exhibit a certain amount of clinically acceptable repeatability with a small bias and variability to one another. In this pilot study we did see an improvement of inter-device variability with DSOCT in comparison to our previous study, ~0.25D vs. ~0.50D [13]. In Fig. 7 it can been seen that the inter-device variability between Topography – DSOCT and DSOCT – Scheimpflug photography was also lower than the variability between Scheimpflug photography – Topography.

OCT benefits from a high axial resolution (<10 μm) independent of sample arm optics and can be developed to have high lateral resolution. Higher axial and lateral resolutions provide more precise estimates for structural boundaries. While we were unable to find the optical axial and lateral resolutions associated with Pentacam, subjectively these appeared lower than our DSOCT system. For OCT, patient motion during the acquisition of a volume is most likely the largest source of error in the acquisition of corneal tomographic data. This motion can be mitigated by acquiring the volume at a faster rate. This was seen previously in the move from a 2 kHz TDOCT system to 26 kHz SDOCT [11,14]. By utilizing a scan pattern with 8 radial meridians across the cornea the total volume acquisition was on the order of hundreds of milliseconds. However, each individual meridian was acquired in 40 ms increasing the effect of motion within a single profile. As previously discussed, we found patient motion to be effectively eliminated at a rate of 100 Hz which corresponds to acquiring a corneal profile in 10 ms. By having only 8 meridians, total acquisition time is reduced but at the expense of spatial sampling at the periphery of the scan pattern. At the edge of the reported 6 mm scan pattern, there is a 1.17 mm linear distance between meridians. By having 20 reconstructed meridians, we reduced the linear distance to 0.47 mm. This more densely sampled scan pattern may offer the capability to accurately analyze higher order optical aberrations beyond spherical aberrations.

It should be noted that the distributed scanning method is adaptable to other targets (i.e., retina, etc.), is independent of wavelength, and is not limited to the specific implementation presented. While this experiment was limited to a 5.04 mm diameter zone, this was a function of system spectral fall-off and low contrast at the corneal periphery and not due to limitations of the scan pattern itself. Switching to an experimental SSOCT source at a longer wavelength could provide the ability to resolve both of those issues. Moving to a higher speed system, such as some experimental SDOCT or SSOCT systems, could offer the ability to both reduce higher frequency motion and sample more densely [18,19,44]. Assuming inertia-limited

#168840 - $15.00 USD Received 21 May 2012; revised 8 Aug 2012; accepted 9 Aug 2012; published 10 Aug 2012

galvanometric mirrors can operate at these high frequencies, DSOCT could be adapted for these experimental systems as well.

To obtain the single curvature values presented above, we applied a best fit sphere to the segmented surfaces of the cornea. This fit averages any higher frequency motion, effectively removing it from the calculation. This also removes any information about higher order aberrations such as coma or astigmatism. In this implementation of DSOCT we were effectively able to sample the patient motion at a rate of ~5 Hz for each meridian. This allows us to know and remove any motion with a temporal frequency of less than 2.5 Hz (i.e., patient breathing or heart beat) across the entire volume. Because we acquired the volumes in ~1 second we have the potential to extend the surface fit to include more than spherical components in the model. Future implementations of DSOCT could potentially be designed to remove higher frequencies of motion and allow for even higher order fits.

5. Conclusion

We have developed a method that reduces the effects of motion during the acquisition of a corneal tomographic volume and shows the potential to accurately recover corneal anterior and posterior curvatures as well as the central corneal thickness. This was demonstrated on two sets of phantoms which in combination addressed all three parameters. DSOCT was applied clinically in a pilot study on normal patients prior to undergoing LASIK refractive surgery. Results were promising in comparisons of DSOCT with both topography and Scheimpflug photography on corneal anterior curvatures and central thicknesses as well as total corneal refractive power calculations. DSOCT also has the potential to be scaled to higher speed systems possibly further reducing the effects of motion.

Acknowledgments

The authors acknowledge financial support from NIH grant R21-EY020001 and by a grant from the Coulter Foundation.

#168840 - $15.00 USD Received 21 May 2012; revised 8 Aug 2012; accepted 9 Aug 2012; published 10 Aug 2012